ADVANCED MATERIALS
www.advmat.de

Embedding Reverse Electron Transfer Between Stably Bare Cu Nanoparticles and Cation-Vacancy $CuWO_4$

Xiyang Wang, Zhen Li, Xinbo Li, Chuan Gao, Yinghui Pu, Xia Zhong, Jingyu Qian, Minli Zeng, Xuefeng Chu, Zuolong Chen, Carl Redshaw, Hua Zhou, Chengjun Sun, Tom Regier, Graham King, James J. Dynes, Bingsen Zhang, Yanqiu Zhu, Guangshe Li, Yue Peng, Nannan Wang,* and Yimin A. Wu**

Cu nanoparticles (NPs) have attracted widespread attention in electronics, energy, and catalysis. However, conventionally synthesized Cu NPs face some challenges such as surface passivation and agglomeration in applications, which impairs their functionalities in the physicochemical properties. Here, the issues above by engineering an embedded interface of stably bare Cu NPs on the cation-vacancy $CuWO_4$ support is addressed, which induces the strong metal-support interactions and reverse electron transfer. Various atomic-scale analyses directly demonstrate the unique electronic structure of the embedded Cu NPs with negative charge and anion oxygen protective layer, which mitigates the typical degradation pathways such as oxidation in ambient air, high-temperature agglomeration, and CO poisoning adsorption. Kinetics and in situ spectroscopic studies unveil that the embedded electron-enriched Cu NPs follow the typical Eley-Rideal mechanism in CO oxidation, contrasting the Langmuir-Hinshelwood mechanism on the traditional Cu NPs. This mechanistic shift is driven by the Coulombic repulsion in anion oxygen layer, enabling its direct reaction with gaseous CO to form the easily desorbed monodentate carbonate.

1. Introduction

Cu NPs have garnered intense interest as viable substitutes for noble metals due to their abundance, cost-effective, and superior physicochemical properties, finding extensive applications in optics, electronics, and catalysis.[1–3] Despite their potential, the inherent instability of metallic Cu NPs leads to the detrimental oxidation in ambient conditions and the agglomeration in heterogeneous catalysis, severely reducing the electron conductivity and hampering the catalytic activity, respectively.[1,4–7] Therefore, it attracts lots of attention to the design and synthesis of Cu NPs with good dispersion, anti-oxidation, and anti-aggregation. It's well-known that the oxidation of metal surfaces can be described by the Cabrera-Mott model, where surface electron migration and interaction with anions oxygen result in a passivating metal-oxide

X. Wang, Z. Li, C. Gao, X. Chu, Y. Peng
School of Environment
Tsinghua University
Beijing 100084, P. R. China
E-mail: pengyue83@tsinghua.edu.cn

X. Wang, Z. Chen, Y. A. Wu
Department of Mechanical and Mechatronics Engineering
Waterloo Institute for Nanotechnology
University of Waterloo
Waterloo, ON N2L 3G1, Canada
E-mail: yimin.wu@uwaterloo.ca

The ORCID identification number(s) for the author(s) of this article can be found under https://doi.org/10.1002/adma.202412570

DOI: 10.1002/adma.202412570

Z. Li, M. Zeng, Y. Zhu, N. Wang
School of Resources
Environment and Materials
Guangxi University
Nanning 530004, P. R. China
E-mail: wangnannan@gxu.edu.cn

X. Li, J. Qian, G. Li
State Key Laboratory of Inorganic Synthesis and Preparative Chemistry
College of Chemistry
Jilin University
Changchun 130012, P. R. China

Y. Pu, X. Zhong, B. Zhang
Shenyang National Laboratory for Materials Science
Institute of Metal Research
Chinese Academy of Sciences
Shenyang 110016, P. R. China

C. Redshaw
Plastics Collaboratory
Department of Chemistry
University of Hull
Hull HU6 7RX, UK

layer.[8,9] Through modifying the surface excess electrons to suppress metal ionization, the Cu nanowires functionalized by $[Cu(\mu\text{-}HCOO)(OH)_2]_2$ short chain of ligands and Cu NPs deposited onto $[Gd_2C]^{2+}\cdot 2e^-$ support with weak interactions showed good oxidation resistance in ambient conditions and remarkable catalytic property.[5,6] Differently, the sintering of Cu NPs usually comply with a process called Ostwald ripening, where the dissolution and atom migration of smaller particles facilitate the consequent growth of larger ones on the support surface.[10,11] Consequently, the anti-aggregated Cu NPs requires a special strong geometry interface, for example, the reverse ripening and encapsulation technologies.[12–14] Traditional designs of anti-aggregated Cu NPs predominantly revolve around coating with stable materials (e.g., long-chain thiolate ligands, epoxy matrix, SiO_2, and TiO_2).[7,14–17] Although these coatings can inhibit oxidation and maintain structural integrity, they severely impair the electron transport and occlude the catalytic sites. Up to now, the development of uncoated and anti-aggregated Cu NPs with surface excess electrons remains a significant challenge, crucial for enhancing the electronic and catalytic properties in actual applications.

In the realm of materials design, the in situ non-stoichiometric exsolution methodology can improve the dispersion, reduce the particle size, enhance the anti-sintering property of bare metal NPs by virtue of the strong embedded interface. The conventional non-stoichiometric exsolution process is represented as $AB_{1+x}O_3 \rightarrow x$B metal NPs + ABO_{3-y}.[18,19] Unfortunately, the stable stoichiometric support difficultly donates more electrons to metal NPs, resulting in the inability to obtain the Cu NPs with surface excess electrons. Drawing from the experience in preparing precious metals with surface excess electrons (Pt, Ir, Ru, Au, etc.), the support enriched with surface anions or containing some cation vacancies can facilitate the reverse electron transfer, for example, carbon materials doping S and Cl anion elements and $Ni_{vac}Fe_{vac}$-layered double hydroxides.[20–24] Here, we first develop an in situ stoichiometric exsolution strategy to prepare the bare metal NPs with a strong embedded interface and tailor a support rich in cation vacancies, fostering the reverse electron transfer as depicted by $CuWO_4 \rightarrow$ xCu NPs with surface excess electrons + Cu-vacancy $Cu_{1-x}WO_4$. This interface design does not require the additional surface passivation or modification, but can yield stable, uncoated Cu NPs with a surplus of surface electrons.

In order to promote the catalytic applications of stable Cu NPs with surface excess electrons, CO oxidation as model reaction is used to identify its chemical properties, including active sites, reaction pathways, and the key intermediates. Herein, various *operando* characterizations such as X-ray absorption spectroscopy (XAS), reaction kinetics, diffuse reflectance infrared Fourier transformations spectroscopy (DRIFTS), and isotope labeling mass spectrometry are employed to track the dynamical structure evolutions and reaction mechanism of tailored and conventional Cu NPs during the reactions for clarifying the influence of interface charge state on the catalytic property. Traditionally deposited $Cu^{\delta+}$ NPs mainly produce stable bidentate carbonate species, complying with the Langmuir-Hinshelwood (L-H) mechanism. In contrast, the surface of electron-enriched Cu NPs is covered by active anion oxygen species due to the Coulomb effect, resulting in the special Eley-Rideal (E-R) mechanism. Therefore, the exsolved Cu NPs with excess electrons manifest the outstanding resistance of CO poisoning, excellent activity, and long-term durability. Atomic-scale understanding of such structure-property relationships will provide new opportunities for the development and commercial application of Cu NPs in various fields, including water-gas shift reaction, CO_2 hydrogenation, electrochemical CO_2 reduction, sensors, and electronic devices.

2. Results and Discussion

2.1. Design and Synthesis of Stably Bare Cu NPs

We design an in situ stoichiometry exsolution route of $CuWO_4$ to prepare the bare and stable Cu NPs with surface excess electrons and good dispersity. The reaction formula is: $CuWO_4 \rightarrow$ xCu NPs with surface excess electrons + $Cu_{1-x}WO_4$ with electron-donating ability, where Cu NPs are embedded into support lattice. Theoretical models of exsolved and deposited interfaces were constructed and optimized to predict the probability of the interface geometric structure regulation through density functional theory (DFT) calculations (**Figure 1a**). $CuWO_4$ support was first prepared using the hydrothermal method.[25] The obtained yellow-green powders were calcined at 600 °C. The exsolved sample, referred to as $Cu/CuWO_4$, was then prepared at 300–350 °C under a H_2 atmosphere utilizing the in situ exsolution method.[26,27] In contrast, a conventional deposition method yielded the comparative $Cu\text{-}CuWO_4$, where Cu NPs were impregnated onto the $CuWO_4$ support surface.[28]

The TEM images reveal a distinct socket interface for the $Cu/CuWO_4$ (Figure 1b,c), displaying uniformly dispersed Cu NPs embedded within the support structure, with sizes ranging from 5 to 20 nm. The $Cu\text{-}CuWO_4$, on the other hand, exhibits a more regular contact interface (Figure S1, Supporting Information).[19,29] After thermal treatment at 350 °C in 5 hours under H_2 atmosphere, scanning electron microscopy (SEM) images (Figures S2,S3, Supporting Information) indicate a transformation from smooth to rough surfaces on both catalysts, with the $Cu\text{-}CuWO_4$ catalyst showing a tendency toward greater particle agglomeration. The TEM-EDS mapping (Figure S4, Supporting Information) confirms the identity of surface Cu NPs. In situ TEM images are employed to elucidate the stoichiometric exsolution process of Cu NPs, as detailed in Figure 1d–i. Observations during the hydrogenation process unveil the notable morphological changes on the $CuWO_4$ support surface; initially, the smooth surface becomes rough within the first 30s. Subsequently, a thin surface amorphous layer appeares to precipitate from localized regions. At 120s, this amorphous layer has enveloped the $CuWO_4$ support. Notably, at 180s, surface reconstruction initiates, leading to the nucleation of Cu NP

H. Zhou, C. Sun
Advanced Photon Source
Argonne National Laboratory
Lemont, IL 60439, USA
T. Regier, G. King, J. J. Dynes
Canadian Light Source
Saskatoon SK S7N 2V3, Canada

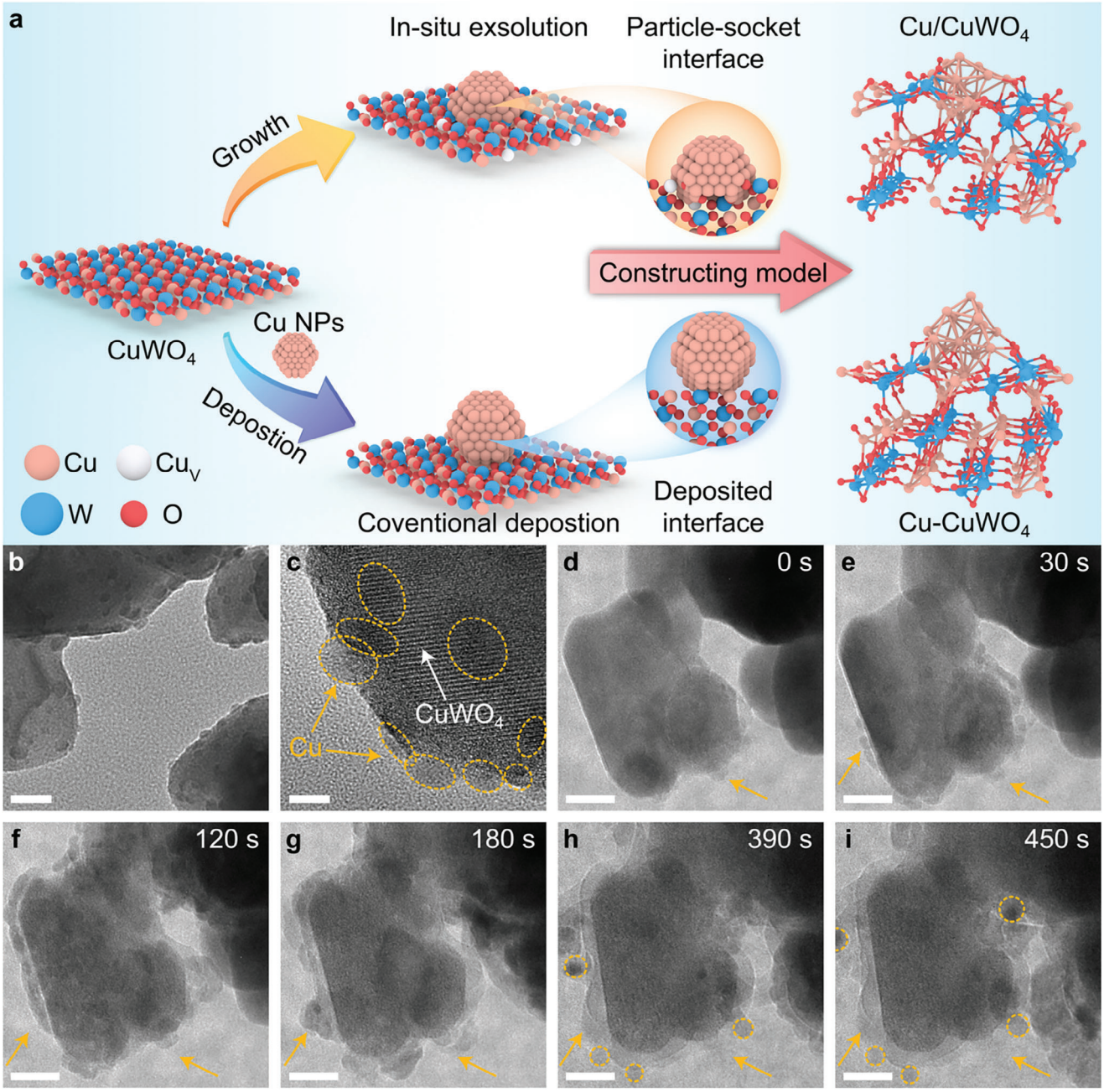

Figure 1. Preparation of stably bare Cu NPs with negative charge. a) Schematic design route for traditionally deposited and socket metal-oxide interface. Interfacial geometry and atomic structure models are built and optimized by DFT calculations. b) TEM images and c) HRTEM images of $Cu/CuWO_4$ kept in air for one month, where the distance scales are 20 nm and 5 nm, respectively. In situ TEM images of $Cu/CuWO_4$ under 10% H_2/He atmosphere for d) 0 s, e) 30 s, f) 120 s, g) 180 s, h) 390 s, and i) 450 s, where the yellow circles represent the exsolved Cu NPs and the distance scale is 20 nm.

seeds. After 390s, the exsolved Cu NPs are uniformly embedded within the $CuWO_4$ support, demonstrating a socket interface appeares. In 60s, minor alterations are observed in the physical position and the size of Cu NPs near the interface, indicative of ongoing dynamic reconstruction. The presence of exsolved Cu NPs and Cu vacancies within the $Cu/CuWO_4$ is substantiated through in situ TEM-EDS mapping (Figure S4, Supporting Information).

2.2. Reverse Electronic Metal-Support Interactions

X-ray diffraction (XRD) patterns are conducted to ascertain the crystal structure of the synthesized Cu NPs and support. The XRD patterns (**Figure** 2a) reveal that both the $Cu\text{-}CuWO_4$ and $Cu/CuWO_4$ exhibit the characteristic face-centered cubic structure of Cu NPs (space group: Fm-3m) and the triclinic phase of $CuWO_4$ (space group: P1), corroborating with previous

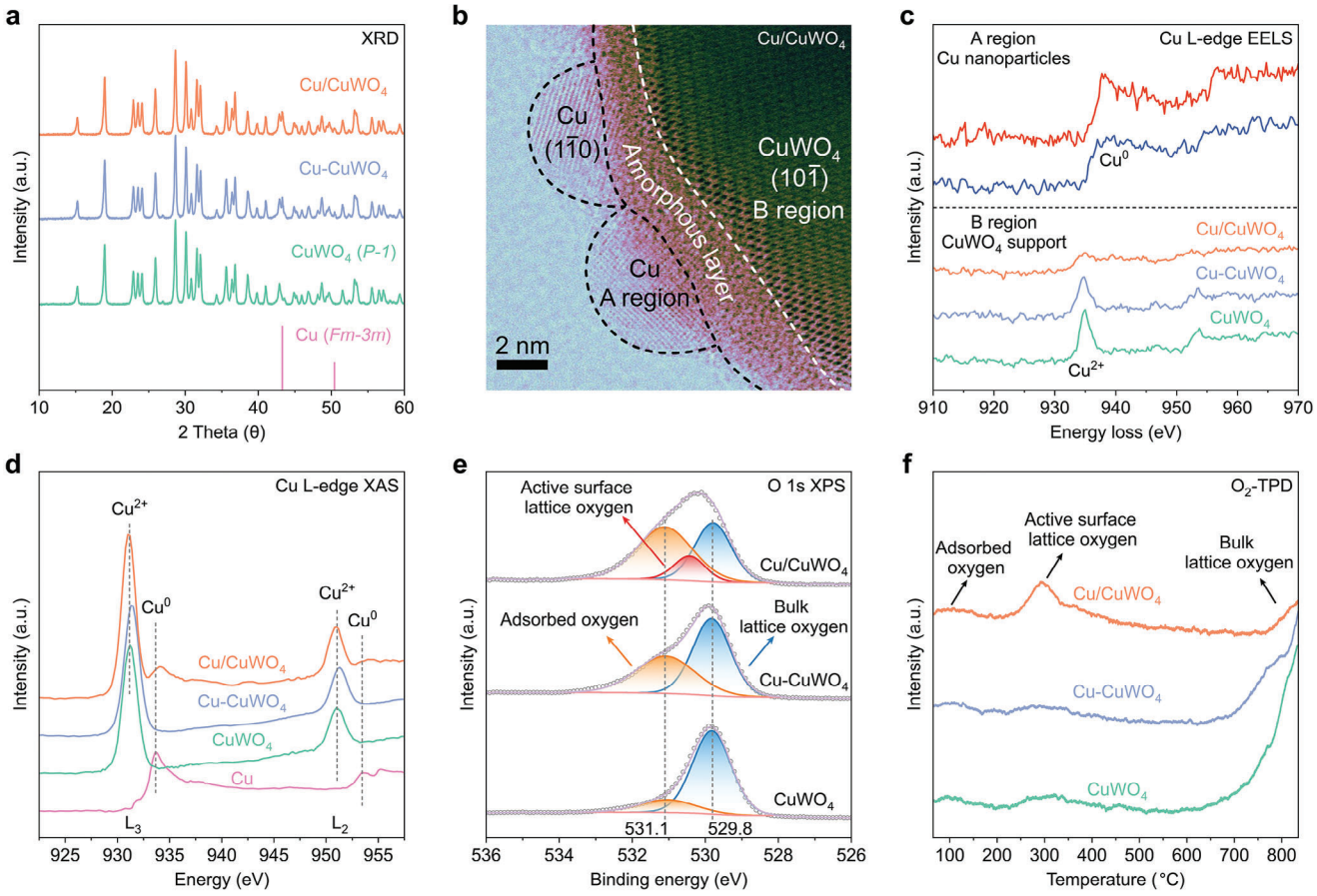

Figure 2. Charge state of Cu NPs and strong interface interactions. a) XRD patterns for $Cu/CuWO_4$, $Cu\text{-}CuWO_4$ and $CuWO_4$. b) LABF-STEM images of $Cu/CuWO_4$. c) Cu L_3-edge EELS spectra of $Cu/CuWO_4$, $Cu\text{-}CuWO_4$ and $CuWO_4$ at different positions. d) Normalized Cu L-edge XAS spectra of $Cu/CuWO_4$, $Cu\text{-}CuWO_4$, $CuWO_4$, and Cu foil. e) O 1s XPS spectra and f) O_2-TPD profiles of $Cu/CuWO_4$, $Cu\text{-}CuWO_4$, and $CuWO_4$. Samples are measured after putting in ambient air for one month.

studies.[25] The enlarged XRD patterns (Figure S5, Supporting Information) show a discernible shift of the (111) peak toward higher angles in $Cu/CuWO_4$ compared to $Cu\text{-}CuWO_4$, implying a reduced interplanar spacing within the (111) planes of the Cu NPs in $Cu/CuWO_4$. The normalized W L_3-edge XANES spectra in Figure S6 (Supporting Information) show that the chemical states of W atom in $CuWO_4$, $Cu/CuWO_4$, and $Cu\text{-}CuWO_4$ are 6+ because they have the same whiteline peak position with WO_3. The atomic-resolution low angle bright field scanning transmission electron microscopy (LABF-STEM) images (Figure 2b) show that the exsolved Cu NPs in $Cu/CuWO_4$ are integrated into the amorphous layer of $CuWO_4$, forming a unique particle-socket interface. The LABF-STEM images of $CuWO_4$ and $Cu\text{-}CuWO_4$ are also shown in Figure S7 (Supporting Information). These images validate their respective pure crystal phases and the nature of the deposited interface, consistent with the XRD and TEM results.

Localized electron energy loss spectroscopy (EELS) is measured to elucidate the electronic state of Cu at the surface or interface of catalysts. Cu L_3-edge EELS spectra in Figure 2c reveal that upon exposure to air for one month, the Cu ions in the support region (region B) of both $Cu/CuWO_4$ and $Cu\text{-}CuWO_4$ retain a typical 2+ oxidation state (Figure S7, Supporting Information). However, a notable discrepancy in Cu content is observed. The $Cu/CuWO_4$ exhibits a significantly lower Cu concentration within the $CuWO_4$, attributable to the intentional introduction of cation vacancies. As known, cation vacancies in $Cu/CuWO_4$ as similar anion ligands donate electrons to the Cu NPs due to metal-support interactions and electron spillovers.[30] Consequently, electron density proximal to the Cu NPs in $Cu/CuWO_4$ (region A) is augmented compared to that in $Cu\text{-}CuWO_4$, evidenced by a higher energy position of the Cu^0 EELS peak.[6,31] Moreover, the presence of oxide layers in Cu NPs of $Cu\text{-}CuWO_4$ is discerned through minor peaks in the O K-edge EELS spectra (Figure S8, Supporting Information). In contrast, the $Cu/CuWO_4$ shows an absence of oxide layers on the Cu NPs surface, affirming a net negative charge transfer from the $CuWO_4$ to Cu NPs and the formation of Cu NPs endowed with excess electrons.

Cu L-edge XAS spectra (Figure 2d) under TEY mode are employed to further probe the surface electronic structure. The absorption peak associated with $Cu/CuWO_4$ is shifted to a higher energy relative to the standard Cu^0 peak in metal Cu NPs, whereas the $Cu\text{-}CuWO_4$ did not display this peak, indicative of surface oxidation of deposited Cu NPs and exsolved Cu NPs with surface excess electrons.[32–34] W 4f XPS spectra in Figure S9a

(Supporting Information) manifest that the W $4f_{7/2}$ peak position of $Cu/CuWO_4$ has a shift to high energy compared with $CuWO_4$ and $Cu\text{-}CuWO_4$. Cu 2p XPS spectra in Figure S9b (Supporting Information) display that Cu^0 peak position of $Cu/CuWO_4$ shifts to lower energy compared to that of $Cu\text{-}CuWO_4$, while the peak position of Cu^{2+} in $Cu/CuWO_4$ shifts to the high energy compared to conventional $Cu\text{-}CuWO_4$. Meanwhile, Cu LMM Auger peak for Cu^0 in $Cu/CuWO_4$ shifts to low energy compared to that in $Cu\text{-}CuWO_4$ (Figure S9c, Supporting Information). These XPS results suggest the reverse electron transfer from cation-vacancy $CuWO_4$ into Cu NPs. In contrast, the Cu L-edge XAS spectra under FY mode probing the bulk structure (Figure S10, Supporting Information) show that $Cu\text{-}CuWO_4$ contains the same Cu^0 absorption peak with metal Cu, confirming the existence and surface oxidation of Cu NPs in $Cu\text{-}CuWO_4$. The shifted Cu^0 peak of exsolved Cu NPs to high energy demonstrate the reverse strong metal-support interactions (SMSI) compared to that of deposited Cu NPs. The decreased crystallinity in the XRD patterns in Cu NPs of $Cu\text{-}CuWO_4$ confirms the deep oxidation of deposited Cu NPs compared with the exsolved Cu NPs. Splitting of peaks a and c in Figure S10 (Supporting Information) stems from the Cu^{2+} in $CuWO_4$ support and surface passivation of supported Cu NPs in $Cu\text{-}CuWO_4$. The reverse SMSI and cation vacancies in $Cu/CuWO_4$ not only amplify the covalency of Cu-O bond (Figure S11, Supporting Information), but also generate novel active oxygen species, such as lattice oxygen (O_{latt}) in the O 1s XPS spectra (Figure 2e).[25,35] In contrast, the interfacial dynamics on $Cu\text{-}CuWO_4$ are found to exert minimal influence on the activity of lattice oxygen (O_{latt}). Notably, the covalency of Cu-O bond experiences a marginal reduction as indicated by an elevated white line intensity (Figure S11, Supporting Information). However, the O_{latt} content in $Cu\text{-}CuWO_4$ is higher in comparison to $CuWO_4$, attributed to the presence of $Cu^{\delta+}$ NPs intrinsic to its structure. The anti-oxidation behavior of exsolved Cu NPs aligns with the reported work regarding Cu NPs that possess surface excess electrons.[6] Our design about the stoichiometric exsolution fabricates the embedded cation-vacancy Cu-oxide interface, which can trigger the surface negative charge through reverse SMSI induced the strong electron spillovers. In $Cu/CuWO_4$ catalyst, the cation-vacancy support is considered as anion ligands to donate some extra electrons to exsolved Cu NPs.

The reactivity of O_{latt} is further investigated using the temperature-programmed desorption of O_2 (O_2-TPD in Figure 2f). The results demonstrate that the $Cu/CuWO_4$ presents a greater quantity of active O_{latt} species at 300 °C relative to both the $CuWO_4$ and $Cu\text{-}CuWO_4$, signifying a potential enhancement in catalytic property and oxygen exchange reactions. The temperature-programmed reduction profiles of H_2 (H_2-TPR in Figure S12, Supporting Information) reveal the higher reducibility of O_{latt} on $Cu/CuWO_4$ compared to that on $CuWO_4$ and $Cu\text{-}CuWO_4$. This increased reducibility and presence of active O_{latt} are likely attributable to the interactive effects between the electron-enriched Cu NPs and the cation-vacancy $CuWO_4$.

To elucidate the SMSI effects in different interfacial geometries, we conduct charge density difference calculations between Cu NPs and support. The results show that the $Cu/CuWO_4$ yielded a higher accumulation of negative charges in comparison to the $Cu\text{-}CuWO_4$ (**Figure 3**a,b; Figure S13, Supporting Information). The spatial distribution of surface charges on $Cu/CuWO_4$ is observed to be considerably more extensive than that on $Cu\text{-}CuWO_4$, a phenomenon attributable to the SMSI facilitated by the unique particle-socket interface. This particle-socket interface markedly tunes the surface electronic structure of both Cu NPs and supports. The role of interface is critical in enhancing the spatial dispersion and bestowing anti-oxidation and anti-aggregation properties to the electron-enriched Cu NPs.

To investigate the atomic structure and SMSI in the Cu NPs with varying electronic charges, we conduct the analyses using extended X-ray absorption fine structure (EXAFS) spectra of Cu K-edge and W L-edge, coupled with operando X-ray pair distribution function (PDF). The K-space Fourier-transformed functions ($k^3\chi(k)$) from the EXAFS spectra of the Cu K-edge and W L_3-edge (Figure S14, Supporting Information) exhibit the similar oscillatory patterns with a high signal-to-noise ratio, suggesting the main structure of these catalysts are similar. The R-space Fourier-transformed functions ($k^3\chi(k)$) from the Cu K-edge EXAFS spectra (Figure 3c) reveal that the $Cu/CuWO_4$ possesses a longer Cu-O bond relative to the $CuWO_4$ and $Cu\text{-}CuWO_4$ due to the formation of Cu vacancies. Conversely, the Cu-Cu bond distances in $Cu/CuWO_4$ are shorter than those in $Cu\text{-}CuWO_4$ because of electron enrichment around the Cu NPs.

Different from the local structure around Cu, both the W-O bond distance in the first shell and W-W/O/Cu bond distances in the second shell exhibit adverse variations. The distance order of W-O bond follows the sequence of $Cu/CuWO_4 < CuWO_4 < Cu\text{-}CuWO_4$ (Figure 3d). The detailed fitting results about Cu K-edge and W L_3-edge EXAFS spectra are summarized in Tables S1,S2 (Supporting Information). An analysis of coordination numbers illuminates the disparities. The $Cu/CuWO_4$ exhibits lower coordination numbers for both Cu (3.86) and W (5.86) atoms compared to the $CuWO_4$ (Cu: 3.96, W: 5.95) and $Cu\text{-}CuWO_4$ (Cu: 3.92, W: 5.91). These deviations stem from Cu vacancies and the embedded interfacial effect, substantiating a higher structural disorder in $Cu/CuWO_4$. These results align with above observations and underscore the impact of negative and positive charge transfers on the chemical environment of Cu and W atoms in catalysts.

Figure 3e illustrates the room temperature X-ray scattering pathways. Due to the significantly higher atomic number of W compared to Cu, the Cu-O scattering signal from $CuWO_4$ is typically overshadowed by the signal of W-centric local structure. According to the theoretical simulation (Figure S15, Supporting Information), these peaks in X-ray PDF spectra can be assigned to the W/Cu-O pairs of $CuWO_4$ at 1.87 Å and the Cu-Cu pair of Cu NPs at 2.50 Å, respectively. To elucidate the temperature-dependent behavior of active sites, the W/Cu-O and Cu-Cu distances within the samples are assessed under varying thermal conditions (Figures S15–S17, Supporting Information). An increase in reaction temperature leads to a notable contraction of the metal-oxygen pairs in $Cu/CuWO_4$, which is not observed in $CuWO_4$ and $Cu\text{-}CuWO_4$. This contraction is hypothesized to arise from the desorption of O_{latt} or a reduction in the coordination numbers of metal-oxygen pairs at the Cu-vacancies $Cu/CuWO_4$. Figure 3f displays the lower onset temperature for the expansion of Cu-Cu distance in $Cu/CuWO_4$. Such expansion is indicative of substantial electron transfer and reconstruction events occurring on the electron-enriched Cu NPs, potentially facilitating the O_{latt} activation. The results above collectively suggest that the SMSI, driven by the particle-socket interface, serves

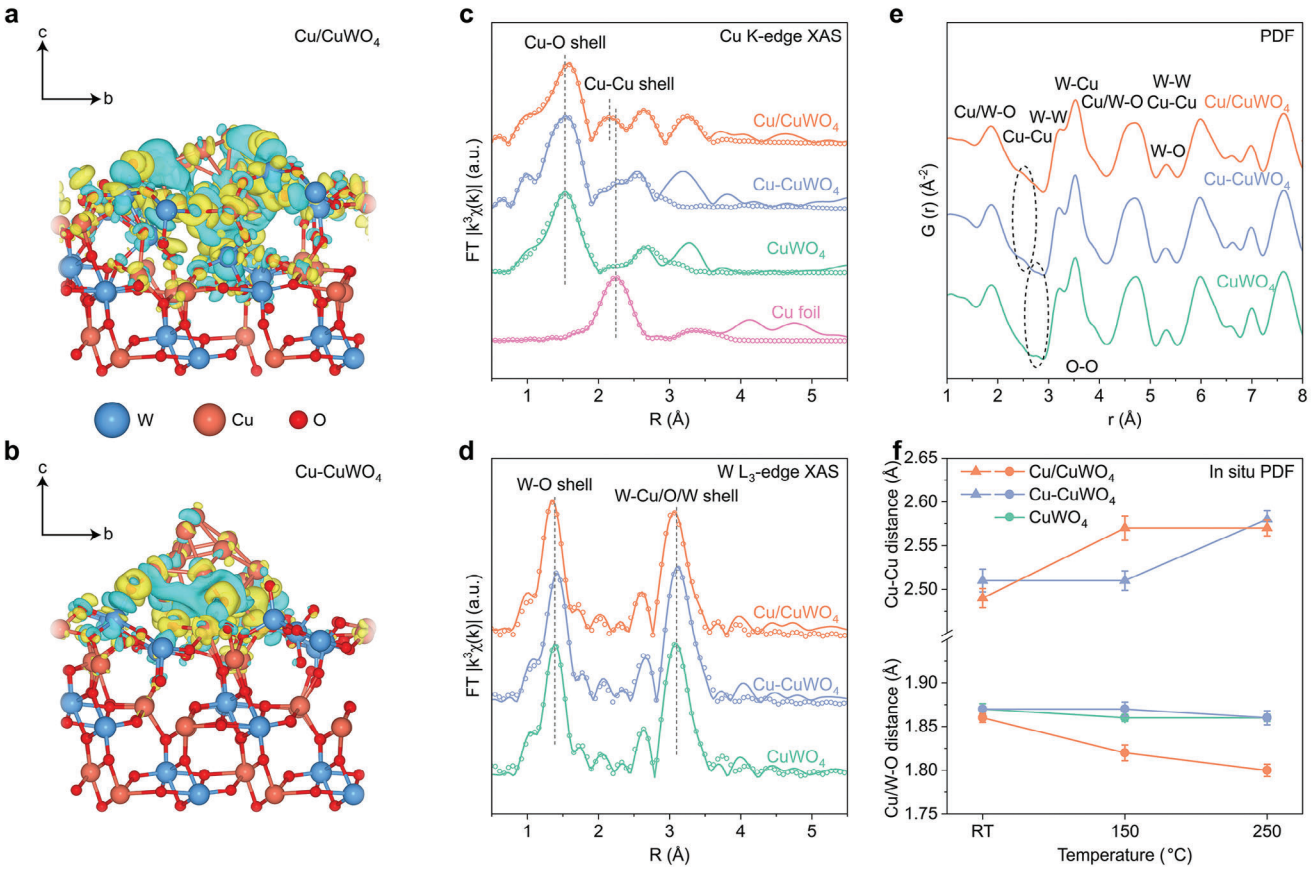

Figure 3. Atomic and electronic structure of Cu NPs. Side views of the charge density difference between Cu NPs and support on a) $Cu/CuWO_4$ and b) $Cu\text{-}CuWO_4$. Yellow and blue green denote the positive and negative charge, respectively. c) R-space Fourier-transform EXAFS spectra of Cu K-edge for $Cu/CuWO_4$, $Cu\text{-}CuWO_4$, $CuWO_4$ and Cu foil. d) R-space Fourier-transform EXAFS spectra of W L_3-edge for $Cu/CuWO_4$, $Cu\text{-}CuWO_4$ and $CuWO_4$. e) Pair Distribution Function (PDF) analysis of $Cu/CuWO_4$, $Cu\text{-}CuWO_4$, and $CuWO_4$ at room temperature. f) Dynamic changes of Cu-O distance in $CuWO_4$ support and Cu-Cu distance in Cu NPs at different temperatures, where the results are obtained from operando PDF analysis.

to refine the atomic structure of both the electron-enriched Cu NPs and the cation-vacancy $CuWO_4$. Consequently, this leads to an enhanced capacity for low-temperature O_{latt} activity, affirming the value of the particle-socket interface in the optimization of active-site structure.

Cu L-edge XAS spectra using FY mode, X-ray PDF spectra, and Cu K-edge EXAFS spectra are conducted to define their contents of Cu NPs in catalysts through fitting and evaluating the amount ratio of Cu-Cu metal bond/Cu—O bond, W—O bond. Cu L-edge XAS spectra in Figure S10 (Supporting Information) show that the Cu ratios of $Cu/CuWO_4$ and $Cu\text{-}CuWO_4$ are 6.8% and 7.4%, respectively. Cu K-edge EXAFS spectra display that the Cu ratios of $Cu/CuWO_4$ and $Cu\text{-}CuWO_4$ are 6.3% and 6.7%, respectively. X-ray PDF spectra manifest that the Cu ratios of $Cu/CuWO_4$ and $Cu\text{-}CuWO_4$ are 3.8% and 4.1%, respectively. Lower value for Cu ratio in PDF data mainly stems from the strong scattering of weight element W. But the close ratio confirms the same supported content of Cu NPs. These results also agree well with the TEM-EDS result about the ≈6% (±1%) loading value of Cu NPs. Similar loading value of Cu NPs on the $CuWO_4$ support surface can be used to well understand the structure-activity relationships.

2.3. Dynamic Structure Evolutions of Cu NPs

To unravel the structure evolutions and dynamic effect of positively or negatively charged Cu NPs during the CO oxidation, we perform the in situ XAS spectra at both O K-edge and Cu L-edge under CO and CO/O_2 atmospheres, respectively.[36] The normalized O K-edge and Cu L-edge XAS spectra are depicted in Figures S18–S23 (Supporting Information). These spectra are transformed into visualized curves, juxtaposing electronic structure against reaction conditions to monitor the structural transitions of the active sites in real-time. The electronic structure is primarily deduced by examining the position and intensity of the XAS absorption peaks.[35,37–39] Under vacuum and solely CO atmospheres, the covalency of Cu-O bond for both $CuWO_4$ and $Cu\text{-}CuWO_4$ remains unchanged (**Figure 4a**). However, upon the introduction of CO, a pronounced weakening in Cu-O bond for $Cu/CuWO_4$ is observed, demonstrated by the shift of the absorption peak to higher energies, an effect that persisted even when the temperature is elevated to 150 and 250 °C. These observations suggest that the reverse SMSI phenomena actively participate in O_{latt} activation at $Cu/CuWO_4$ interface. In $CO + O_2$ atmospheres, a more significant low-energy shift in peak positions is

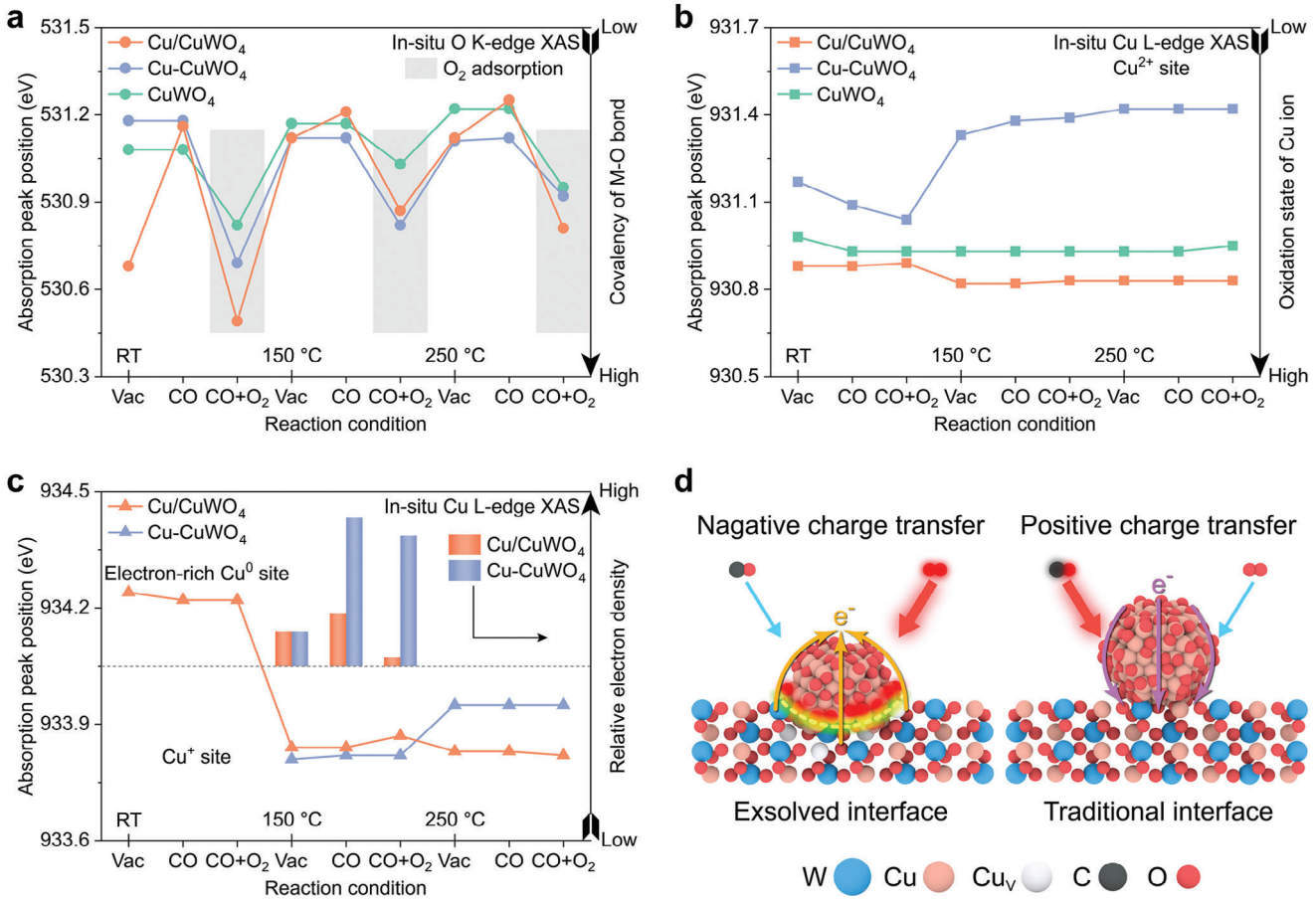

Figure 4. Dynamic evolution of electronic structure of Cu NPs. Dynamic evolutions of a) surface adsorbed O_2 and metal-oxygen bond covalency over $Cu/CuWO_4$, $Cu\text{-}CuWO_4$ and $CuWO_4$, where the covalency is clarified by peak A position in O K-edge XAS spectra of Figures S18–S20 (Supporting Information). b) oxidation state of Cu^{2+} ions over $Cu/CuWO_4$, $Cu\text{-}CuWO_4$ and $CuWO_4$, where it is assessed by peak A position in Cu L-edge XAS spectra of Figures S21–S23 (Supporting Information). c) Valence state variations and relative electron density of $Cu/CuWO_4$ and $Cu\text{-}CuWO_4$ under kinetic reaction conditions, where they are evaluated via the position and white line intensity of peak B in Cu L-edge XAS spectra of Figures S21–S23 (Supporting Information). d) Schematic diagram of SMSI in exsolved and deposited interfaces.

noted for $Cu/CuWO_4$ compared to $CuWO_4$ and $Cu\text{-}CuWO_4$, indicating that the electron-enriched Cu NPs enhance oxygen adsorption at the active sites, potentially leading to the formation of an anion oxygen protective layer. As the reaction temperature for CO oxidation is increased, the downward shift in the O K-edge spectra became less pronounced, implying that gaseous O_2 interaction with both $Cu/CuWO_4$ and $Cu\text{-}CuWO_4$ can be further activated above 150 °C.

As for the valence state of Cu (Figure 4b), we observe divergent trends as a function of temperature. For $Cu/CuWO_4$, the Cu valence state increases with the temperatures, whereas it diminishes on $Cu\text{-}CuWO_4$, signifying disparate electron transfer dynamics in the SMSI. Surface structural changes of Cu NPs during the reaction are also monitored (Figure 4c). At ambient temperatures, the $Cu\text{-}CuWO_4$ is found to be fully passivated by oxidation layers, evidenced by the absence of characteristic peaks. This passivation increases the CO competitive adsorption, inhibiting the oxygen activation. Conversely, the $Cu/CuWO_4$, endows with surplus surface electrons, are capable of forming an anion oxygen protective layer while maintaining a metal surface state with excess electrons. These findings imply that the SMSI manifests in antipodal directions of charge transfer between the electron-enriched Cu NPs and the cation-vacancy $CuWO_4$ (Figure 4d). Above 150 °C, the Coulombic effect enhances oxygen adsorption and subsequent dissociation on the electron-enriched Cu NPs of $Cu/CuWO_4$ due to negative charge transfer. In contrast, positive charge transfer on $Cu\text{-}CuWO_4$ facilitates the desorption of stable surface oxygen species from the $Cu^{\delta+}$ NPs and robust competitive CO adsorption, leading to a reduced oxidation state. The predilection for redox reactions is governed by the electron transfer, making the $Cu\text{-}CuWO_4$ susceptible to CO poisoning and formation of stable bidentate carbonates, whereas the $Cu/CuWO_4$ becomes enveloped by adsorbed oxygen species.

Finally, to gauge the relative electron density at the Cu sites within Cu NPs at 150 °C, kinetic conditions are employed, as effects from the support remain influential at 250 °C.[40] The histogram in Figure 4c delineates the dynamic shifts in electron density of Cu NPs under CO and CO/O_2 conditions, aiding in the dissection of CO and O_2 adsorption capacities. It is noted that

reductive CO preferentially adsorbs onto Cu-$CuWO_4$ due to more positive charge on Cu NPs surface. The interactions between CO and Cu NPs of Cu-$CuWO_4$ culminate in a marked elevation of electron density at the $Cu^{\delta+}$ NPs. In contrast, the Cu/$CuWO_4$ undergoes a swift alteration from an increase (under CO) to a decrease (under CO/O_2) in relative electron density, suggesting that the electron-enriched Cu NPs of Cu/$CuWO_4$ predominantly attract O_2 over CO.

In situ TEM images in Figure S24 (Supporting Information) show that Cu/$CuWO_4$ surface contains thin CuO_x layer (CuO_x@Cu: core-shell structure) due to the oxidative atmosphere at 250 °C, resulting in the typical E-R mechanism CO directly reacting with oxygen adsorbed on exsolved Cu NPs surface. When the reactive gas is pumped into vacuum condition, the Cu/$CuWO_4$ resumes the original microstructure due to strong reducing effect of electron beam irradiation at high temperatures. Furthermore, Cu L-edge XAS spectra of Cu/$CuWO_4$ and reacted Cu/$CuWO_4$ under FY mode (Figure S25, Supporting Information) are also conducted to observe the electronic structure of Cu NPs in the reacted Cu/$CuWO_4$. Increased peak a (Cu^{2+}) and decreased peak b (mixed Cu^0 and Cu^+) confirm the surface oxidation and oxygen adsorption during the catalytic process. In contrast, traditional CuO_x@Cu-$CuWO_4$ catalyst easily occurring the CO poisoning adsorption due to the positive electron transfer. Therefore, the important difference of catalytic mechanism and property between deposited Cu NPs and exsolved Cu NPs stems from the surface electron structure of CuO_x layers on Cu NPs, namely positive and reverse electron transfer during the catalytic reactions.

DFT calculations are employed to quantify the adsorption energies of O_2 and CO on the Cu NPs (Figure S26, Supporting Information). The Cu/$CuWO_4$ demonstrates a higher affinity for O_2 adsorption (−1.14 eV) compared to the Cu-$CuWO_4$ (−0.97 eV), while CO adsorption on Cu/$CuWO_4$ is less favored (−0.79 eV versus −0.88 eV). This differential adsorption profile can be attributed to the Coulombic interactions between the electron-enriched Cu NPs and O_{latt}, facilitating enhanced oxygen adsorption but restricting oxygen penetration into the bulk lattice, thereby conferring superior anti-oxidation properties to Cu/$CuWO_4$.[6] With increasing the temperature, the Cu/$CuWO_4$ becomes fully saturated with active oxygen species, and the presence of excess electrons impeds the adsorption of CO, consequently yielding distinct intermediates and mechanisms in CO oxidation relative to Cu-$CuWO_4$.

2.4. Reaction Mechanisms of Cu NPs in CO Oxidation

To investigate the effect of surface charge states of Cu NPs on reaction pathways, in situ DRIFTS spectra of Cu/$CuWO_4$ and Cu-$CuWO_4$ are employed. According to previous works, the intermediate species can be attributed to monodentate carbonate (α, 1343, 1445, and 1508 cm^{-1}), bidentate carbonate (β, 1324, 1544, 1599, and 1683 cm^{-1}), bridged adsorbed Cu-CO (γ, 1804 and 1917 cm^{-1}), linearly adsorbed Cu-CO (δ, 2117 cm^{-1}), gaseous CO (2184 cm^{-1}), and gaseous CO_2 (2338 and 2360 cm^{-1}), respectively (Table S3, Supporting Information).[41–45]

The Cu/$CuWO_4$ has a small redshift to high wavenumbers in Cu-CO vibrations compared to the Cu-$CuWO_4$. Upon the co-introduction of CO and O_2, a reversal in peak frequency from 2119 to 2111 cm^{-1} is noted, evidencing a blueshift effect consistent with the positive charge influence of Cu NPs on CO adsorption. Furthermore, differential adsorptive behaviors are revealed by the strong peak of bridged Cu-CO and carbonate species at 200 °C in Cu/$CuWO_4$, which are absent in $CuWO_4$ and Cu-$CuWO_4$ (**Figure 5a**). This suggests that O_{latt} in Cu/$CuWO_4$ is activated via SMSI, then adsorbed CO reacts with O_{latt} to yield monodentate and bidentate carbonates (Mars-van Krevelen (MvK) mechanism). A comparative low peak for Cu-CO and a high intensity for CO on Cu/$CuWO_4$ also indicates that the electron-enriched Cu NPs mitigate CO poisoning. When the atmosphere is switched solely to O_2 (Figure 5b), the Cu-$CuWO_4$ surface is predominantly populated by stable bidentate carbonates, while the Cu/$CuWO_4$ surface favors the formation of monodentate carbonates and CO_2. Consequently, Cu/$CuWO_4$ exhibits enhanced activity and stability in CO oxidation due to the dominant active sites on the electron-enriched Cu NPs and a supportive effect that augments negative charge transfer. When CO and O_2 are both introduced, an increase in bidentate carbonates is observed for Cu-$CuWO_4$ compared to individual CO or O_2 condition, whereas, the Cu/$CuWO_4$ shows the negligible bidentate carbonate species (Figure 5c). To further prove the chemical property of monodentate and bidentate carbonate species, the time-resolved in situ DRIFTS spectra over Cu-$CuWO_4$ and Cu/$CuWO_4$ at 200 °C are measured under the different atmospheres. Figure S27a (Supporting Information) shows that the Cu-$CuWO_4$ mainly adsorbs bidentate carbonate species. With increasing pump time of CO gas, the decreased bidentate carbonate species indicate the poisoning adsorption of CO gas. In the contrast, Cu/$CuWO_4$ mainly adsorbs monodentate carbonate species and surface content of monodentate carbonate species increases with increasing the CO gas (Figure S27b, Supporting Information). CO and O_2 mixed gases are introduced into catalyst surface to observe the variation of carbonate species. Figure S27c (Supporting Information) shows that the bidentate carbonate species adsorbed on the Cu-$CuWO_4$ surface increase under CO and O_2 atmosphere, suggesting that the $Cu^{\delta+}$ NPs stabilize the bidentate carbonate species. Differently, after switched into CO + O_2 atmospheres, the monodentate carbonate species adsorbed on the Cu/$CuWO_4$ surface dramatically reduces, demonstrating that the monodentate carbonate species easily desorb from the electron-enriched Cu NPs surface (Figure S27d, Supporting Information). These in situ FT-IR results imply that the Cu/$CuWO_4$ primarily adheres to the E-R mechanism at the electron-enriched Cu NPs, attributed to the complete coverage by active oxygen species, and a lesser extent of the MvK mechanism at the O_{latt} of support. In contrast, the Cu-$CuWO_4$ demonstrates a variety of mechanisms including the L-H and E-R, stemming from weak oxygen activation, strong CO adsorption, and inefficient carbonate decomposition.

To further clarify the catalytic mechanism, the reaction rates of CO oxidation over Cu/$CuWO_4$ and Cu-$CuWO_4$ are assessed under stringent kinetic control conditions.[40] Temperature-dependent catalytic curves for CO oxidation (Figure S28, Supporting Information) demonstrate that Cu/$CuWO_4$ has the better catalytic activity than Cu-$CuWO_4$ and $CuWO_4$ in 200 °C. Furthermore, the normalized reaction rate by surface specific area (Table S4 and Figure S29, Supporting Information) is used to calculate the reaction orders with respect to CO and O_2. For

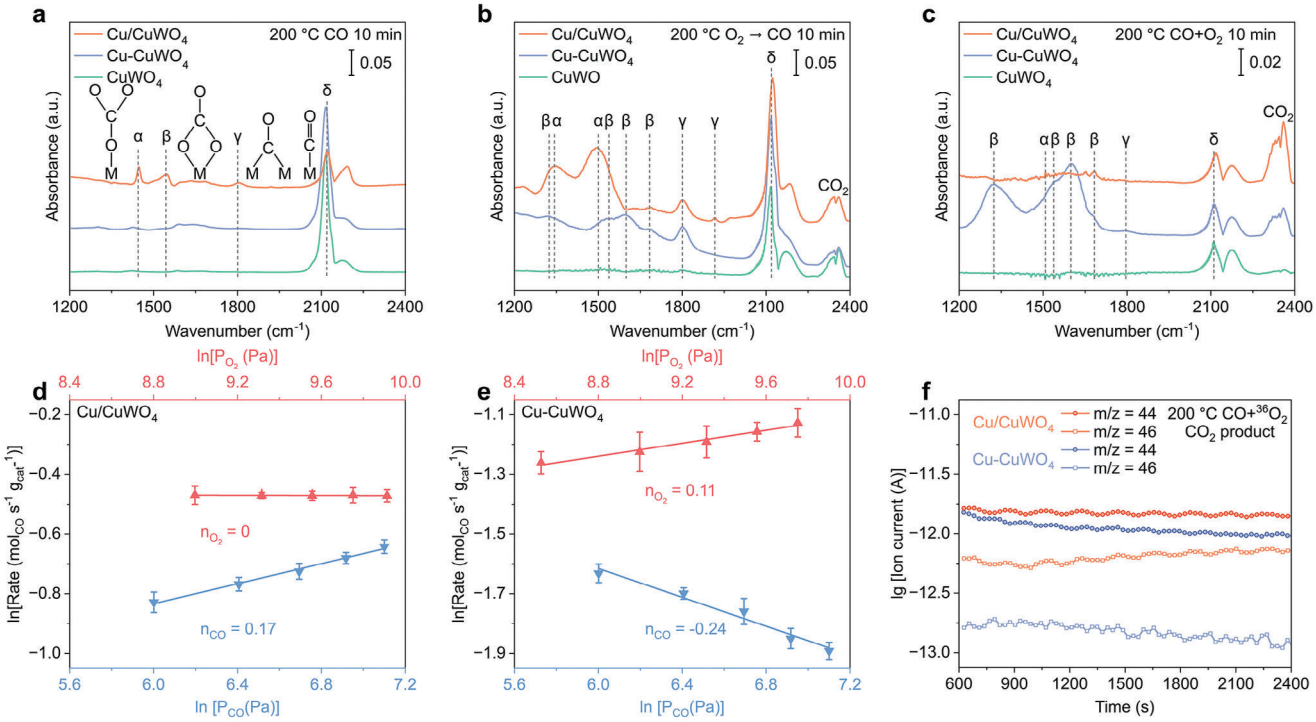

Figure 5. Effect of surface charge state of Cu NPs on reaction mechanism. In situ DRIFTS spectra over $Cu/CuWO_4$, $Cu\text{-}CuWO_4$, and $CuWO_4$ at 200 °C under the atmosphere of a) N_2-CO, b) O_2-CO, and c) CO + O_2. Effect of CO and O_2 partial pressure on the reaction rate over d) $Cu/CuWO_4$ and e) $Cu\text{-}CuWO_4$. Red curve: P_{CO} = 1 kPa, P_{O2} = 5-20 kPa; Blue curve: P_{O2} = 10 kPa, P_{CO} = 0.4-1.2 kPa. f) Time-resolved isotopic $^{36}O_2$ labeled online mass spectrometry over $Cu\text{-}CuWO_4$ and $Cu/CuWO_4$ for CO oxidation.

$Cu/CuWO_4$, reaction orders were determined to be 0.2 for CO and 0 for O_2, whereas the reaction orders for $Cu\text{-}CuWO_4$ were −0.2 for CO and 0.1 for O_2 (Figure 5d,e). The zeroth-order kinetics in O_2 over $Cu/CuWO_4$ implies that adsorbed surface oxygen species are readily activated and participate directly in the oxidation process.[40] The positive reaction order for CO on $Cu/CuWO_4$ indicates that an increased concentration of CO enhances the oxidation rate. These kinetic and in situ DRIFTS results affirm the prevalence of the E-R mechanism in CO oxidation on $Cu/CuWO_4$. The normalized rate and a 40-h stability test also proved that the $Cu/CuWO_4$ possessed a higher CO oxidation rate and durability (Figure S30, Supporting Information). $Cu/CuWO_4$ catalyst also possesses the lower activation energy barrier (55 kJ mol^{-1}) than $Cu\text{-}CuWO_4$, indicating the importance of exsolved interface on tuning the reactivity of active sites (Figure S31, Supporting Information). Table comparing the performance of different catalysts are used to confirm the catalytic property of exsolved $Cu/CuWO_4$ (Table S5, Supporting Information). We directly observe that compared with anti-sintering Pt-based catalysts, this stable exsolved $Cu/CuWO_4$ catalyst shows better catalytic activity of CO oxidation, but its activity is lower than those catalysts easily sintering Cu NPs based catalysts. This work addresses the anti-sinter property of traditional Cu NPs and triggers unique electron structure with negative charge.

In operando isotope-labeled mass spectrometry, the $Cu/CuWO_4$ exhibited a significantly enhanced $^{46}CO_2$ signal compared to the $Cu\text{-}CuWO_4$, indicative of superior catalytic efficiency via the E-R mechanism, utilizing $^{36}O_2$ (Figure 5f). The observed $^{44}CO_2$ signal is comparable for both catalysts, signifying the concurrent presence of reactions involving surface-adsorbed oxygen (L-H/E-R) and O_{latt} (MvK). The activity and availability of O_{latt} on $Cu/CuWO_4$ are higher than on $Cu\text{-}CuWO_4$, which is corroborated by the attenuated rate of decrease in CO oxidation activity. To quantitively analyze the accurate contribution of Cu site in Cu NPs and O_{latt} site in amorphous layer of support, the normalized signals of $^{44}CO_2$ and $^{46}CO_2$ are processed into the real gas concentration. Our concentration calculation results show that the Cu site and O site on $Cu/CuWO_4$ contribute 75% and 25%, respectively. In the contrast, the Cu site and O site on $Cu\text{-}CuWO_4$ in CO oxidation contribute 44% and 56%, respectively. The reactivity of Cu site and O site on $Cu/CuWO_4$ have 1.5 times and 5 times as that on $Cu\text{-}CuWO_4$, respectively. These results are well consistent with CO oxidation kinetics and NAP-XAS spectra. These in situ spectroscopic characterizations clarify the effects of the surface charge state of Cu NPs and the embedded interface on the anti-oxidation and anti-aggregation properties of Cu NPs and reaction intermediates. In additions, cation vacancies in $Cu/CuWO_4$ support not only facilitate the interface transfer between Cu NPs and oxide support, but also improve the activity of surface lattice oxygen in exsolved $CuWO_4$ support.

DFT results (Figures S32–S34, Supporting Information) reveal the lower activation energy barriers (0.53 eV) for the E-R mechanism on $Cu/CuWO_4$ compared to $Cu\text{-}CuWO_4$ (1.15 eV), where CO reacts with the surface-adsorbed oxygen species. Conversely, the negative reaction order for CO on $Cu\text{-}CuWO_4$ indicates a

tendency for CO poisoning, concomitant with adherence to E-R, L-H, and MvK mechanisms. DFT results (Figures S35–S37, Supporting Information) elucidate the heightened reactivity of O_{latt} on Cu/$CuWO_4$ compared to Cu-$CuWO_4$. In the MvK mechanism, the energy barriers for the reaction of adsorbed CO* with O_{latt} were 2.14 eV and 2.70 eV, respectively. The increased $^{46}CO_2$ signal on Cu/$CuWO_4$ proves its stronger oxygen exchange ability.

3. Conclusion

In this work, we successfully synthesized the stably bare electron-rich and anti-aggregated Cu NPs by in situ stoichiometric exsolution of $CuWO_4$. Utilizing CO oxidation as a probe reaction and deploying in situ multimodal characterization techniques, we delineated the pivotal role of interface geometric and electronic structures on the chemical properties of stably bare Electron-enriched NPs: i) The electron-enriched Cu NPs counteract the surface oxidation prevalent in ambient conditions, impede aggregation, and exhibit a preferential CO adsorption compared to the traditional $Cu^{\delta+}$ NPs. ii) Electron-enriched Cu NPs predominantly facilitate the desorption of monodentate carbonate species, whereas the $Cu^{\delta+}$ NPs stabilize bidentate carbonate species. iii) In contrast to the L-H mechanism primarily on the $Cu^{\delta+}$ NPs, the electron-enriched Cu NPs adhere to the E-R mechanism, enabling direct interaction between CO and adsorbed oxygen.

The reverse SMSI effect of exsolved Cu NPs not only stabilizes the electron density at the Cu NPs but also establishes a robust interface that mitigates surface oxidation in ambient air and resists particle aggregation. The enhanced affinity for CO adsorption can be attributed to the formation of an anion oxygen protective layer. Accordingly, the Cu/$CuWO_4$ with the electron-enriched Cu NPs demonstrate the exceptional catalytic activity and durability in CO oxidation. Fine-tuning of interface parameters in supported catalysts emerges as a critical strategy for modulating the reverse SMSI and crafting cutting-edge metal NPs. Our insights into the interface structure-property relationships are anticipated to catalyze novel avenues for the enhancement and broader commercial deployment of supported Cu NPs across various domains, including CO_2 hydrogenation, water-gas shifts, and exhaust control of vehicles.

Supporting Information

Supporting Information is available from the Wiley Online Library or from the author.

Acknowledgements

X.W., Z.L. contributed equally to this work. Y.A.W. thanks the funding from Tang family chair in new energy materials and sustainability, and Natural Science and Engineering Research Council (NSERC) of Canada (RGPIN-2020-05903, GECR-2020-00476). Y.P. acknowledges the financially support from the National Natural Science Foundation of China (T2341002 and 22276104). N.W. thanks National Natural Science Foundation (51972068) and the Natural Science Foundation of Guangxi (2018GXNSFBA138025). The work was also supported by Users with Excellence Program of Hefei Science Center CAS (2020HSC-UE002) and the National Natural Science Foundation of China (U1932211). X.W. and Z.C. acknowledge the receipt of support from the CLSI Student Travel Support Program. These works for NAP-XAS, operando PDF, and Cu K-edge XAFS were performed at SGM, Brockhouse high energy wiggler, and SXRMB beamlines of the Canadian Light Source (CLS), a national research facility of the University of Saskatchewan, which was supported by the Canada Foundation for Innovation (CFI), the Natural Sciences and Engineering Research Council (NSERC), the National Research Council (NRC), and the Government of Saskatchewan. The authors were also thankful for the W L_3-edge XAFS test support of resources from the Advanced Photon Source, a U.S. Department of Energy (DOE) Office of Science user facility operated by the DOE Office of Science by the Argonne National Laboratory under contract no. DE-AC02-06CH11357. The authors thank beamlines MCD-A and MCD-B (Soochow Beamline for Energy Materials) in National Synchrotron Radiation Laboratory (NSRL) for providing beam time. CR thanks the EPSRC for an Overseas Travel Grant.

Conflict of Interest

The authors declare no conflict of interest.

Data Availability Statement

The data that support the findings of this study are available from the corresponding author upon reasonable request.

Keywords

Cu nanoparticles, in situ spectroscopies, metal-support interactions, reverse electron transfer, strong embedded interface

Received: August 23, 2024
Revised: September 12, 2024
Published online:

[1] M. B. Gawande, A. Goswami, F. X. Felpin, T. Asefa, X. Huang, R. Silva, X. Zou, R. Zboril, R. S. Varma, *Chem. Rev.* **2016**, *116*, 3722.
[2] F. Habashi, in *Alloys: Preparation, Properties, Applications*, Wiley, Hoboken, NJ, USA **2008**.
[3] J. Perelaer, P. J. Smith, D. Mager, D. Soltman, S. K. Volkman, V. Subramanian, J. G. Korvink, U. S. Schubert, *J. Mater. Chem.* **2010**, *20*, 8446.
[4] S. J. Kim, Y. I. Kim, B. Lamichhane, Y. H. Kim, Y. Lee, C. R. Cho, M. Cheon, J. C. Kim, H. Y. Jeong, T. Ha, J. Kim, Y. H. Lee, S. G. Kim, Y. M. Kim, S. Y. Jeong, *Nature* **2022**, *603*, 434.
[5] J. Peng, B. L. Chen, Z. C. Wang, J. Guo, B. H. Wu, S. Q. Hao, Q. H. Zhang, L. Gu, Q. Zhou, Z. Liu, S. Q. Hong, S. F. You, A. Fu, Z. F. Shi, H. Xie, D. Y. Cao, C. J. Lin, G. Fu, L. S. Zheng, Y. Jiang, N. F. Zheng, *Nature* **2020**, *586*, 390.
[6] K. Chung, J. Bang, A. Thacharon, H. Y. Song, S. H. Kang, W. S. Jang, N. Dhull, D. Thapa, C. M. Ajmal, B. Song, S. G. Lee, Z. Wang, A. Jetybayeva, S. Hong, K. H. Lee, E. J. Cho, S. Baik, S. H. Oh, Y. M. Kim, Y. H. Lee, S. G. Kim, S. W. Kim, *Nat. Nanotechnol.* **2022**, *17*, 285.
[7] S. Wang, K. Feng, D. K. Zhang, D. R. Yang, M. Q. Xiao, C. C. Zhang, L. He, B. H. Yan, G. A. Ozin, W. Sun, *Adv. Sci.* **2022**, *9*, 2104972.
[8] N. Cabrera, N. F. Mott, *Rep. Prog. Phys.* **1949**, *12*, 163.
[9] V. P. Zhdanov, *Surf. Sci.* **2019**, *684*, 24.
[10] R. van den Berg, T. E. Parmentier, C. F. Elkjær, C. J. Gommes, J. Sehested, S. Helveg, P. E. de Jongh, K. P. de Jong, *ACS Catal.* **2015**, *5*, 4439.

[11] P. Wynblatt, N. A. Gjostein, *Acta Metall.* **1976**, *24*, 1165.
[12] L. Liu, J. Lu, Y. Yang, W. Ruettinger, X. Gao, M. Wang, H. Lou, Z. Wang, Y. Liu, X. Tao, L. Li, Y. Wang, H. Li, H. Zhou, C. Wang, Q. Luo, H. Wu, K. Zhang, J. Ma, X. Cao, L. Wang, F. Xiao, *Science* **2024**, *383*, 94.
[13] D. Yao, Y. Wang, Y. Li, A. Li, Z. Zhen, J. Lv, F. Sun, R. Yang, J. Luo, Z. Jiang, Y. Wang, X. Ma, *Nat. Commun.* **2023**, *14*, 1123.
[14] P. E. Laibinis, G. M. Whitesides, *J. Am. Chem. Soc.* **1992**, *114*, 9022.
[15] G. Dabera, M. Walker, A. M. Sanchez, H. J. Pereira, R. Beanland, R. A. Hatton, *Nat. Commun.* **2017**, *8*, 1894.
[16] L. Wang, L. Wang, X. Meng, F. Xiao, *Adv. Mater.* **2019**, *31*, 1901905.
[17] C. Muhammed Ajmal, A. P. Benny, W. Jeon, S. Kim, S. W. Kim, S. Baik, *Mater. Today* **2021**, *48*, 59.
[18] D. Neagu, G. Tsekouras, D. N. Miller, H. Menard, J. T. Irvine, *Nat. Chem.* **2013**, *5*, 916.
[19] D. Neagu, T. S. Oh, D. N. Miller, H. Menard, S. M. Bukhari, S. R. Gamble, R. J. Gorte, J. M. Vohs, J. T. S. Irvine, *Nat. Chem.* **2015**, *6*, 8120.
[20] Q. Yan, D. Wu, S. Chu, Z. Chen, Y. Lin, M. Chen, J. Zhang, X. Wu, H. Liang, *Nat. Commun.* **2019**, *10*, 4977.
[21] W. Chen, Y. Che, J. Xia, L. Zheng, H. Lv, J. Zhang, H. Liang, X. Meng, D. Ma, W. Song, X. Wu, C. Cao, *J. Am. Chem. Soc.* **2024**, *146*, 11542.
[22] L. Peng, N. Yang, Y. Yang, Q. Wang, X. Xie, D. Sun-Waterhouse, L. Shang, T. Zhang, G. I. N. Waterhouse, *Angew. Chem., Int. Ed.* **2021**, *60*, 24612.
[23] B. P. Hahn, J. W. Long, D. R. Rolison, *Acc. Chem. Res.* **2013**, *46*, 1181.
[24] W. Zhu, Z. Wu, G. S. Foo, X. Gao, M. Zhou, B. Liu, G. M. Veith, P. Wu, K. L. Browning, H. N. Lee, H. Li, S. Dai, H. Zhu, *Nat. Commun.* **2017**, *8*, 15291.
[25] Z. Li, X. Wang, M. Zeng, K. Chen, D. Cao, Y. Huang, Y. Zhu, W. Zhang, N. Wang, Y. A. Wu, *J. Colloid Interface Sci.* **2022**, *625*, 363.
[26] Y. Cong, Z. Geng, Q. Zhu, H. Hou, X. Wu, X. Wang, K. Huang, S. Feng, *Angew. Chem., Int. Ed.* **2021**, *60*, 23380.
[27] T. Ruh, D. Berkovec, F. Schrenk, C. Rameshan, *Chem. Commun.* **2023**, *59*, 3948.
[28] S. Jung, C. Lu, H. He, K. Ahn, R. J. Gorte, J. M. Vohs, *J. Power Sources* **2006**, *154*, 42.
[29] M. Wang, E. I. Papaioannou, I. S. Metcalfe, A. Naden, C. D. Savaniu, J. T. Irvine, *Adv. Funct. Mater.* **2023**, *33*, 2302102.
[30] P. Xiong, F. Zhang, X. Zhang, Y. Liu, Y. Wu, S. Wang, J. Safaei, B. Sun, R. Ma, Z. Liu, Y. Bando, T. Sasaki, X. Wang, J. Zhu, G. Wang, *Nat. Commun.* **2021**, *12*, 4184.
[31] Z. L. Wang, *Adv. Mater.* **2003**, *15*, 1497.
[32] H. Liu, J. Guo, Y. Yin, A. Augustsson, C. Dong, J. Nordgren, C. Chang, P. Alivisatos, G. Thornton, D. F. Ogletree, F. G. Requejo, F. de Groot, M. Salmeron, *Nano Lett.* **2007**, *7*, 1919.
[33] A. M. Abdel-Mageed, A. Klyushin, A. Rezvani, A. Knop-Gericke, R. Schlögl, J. Behm, *Angew. Chem., Int. Ed.* **2019**, *58*, 10325.
[34] M. L. Baker, M. W. Mara, J. J. Yan, K. O. Hodgson, B. Hedman, E. I. Solomon, *Coord. Chem. Rev.* **2017**, *345*, 182.
[35] X. Wang, Z. Pan, X. Chu, K. Huang, Y. Cong, R. Cao, R. Sarangi, L. Li, G. Li, S. Feng, *Angew. Chem., Int. Ed.* **2019**, *58*, 11720.
[36] Y. Zhu, J. Wang, S. B. Patel, C. Li, A. R. Head, J. A. Boscoboinik, G. Zhou, *Proc. Natl. Acad. Sci. USA* **2023**, *120*, 2215189120.
[37] J. W. Smith, R. J. Saykally, *Chem. Rev.* **2017**, *117*, 13909.
[38] K. Zhu, Q. Zhu, M. Jiang, Y. Zhang, Z. Shao, Z. Geng, X. Wang, H. Zeng, X. Wu, W. Zhang, K. Huang, S. Feng, *Angew. Chem., Int. Ed.* **2022**, *61*, 202207600.
[39] M. Zeng, X. Wang, Q. Yang, X. Chu, Z. Chen, Z. Li, C. Redshaw, C. Wang, Y. Peng, N. Wang, Y. Zhu, Y. A. Wu, *ACS Appl. Mater. Interfaces* **2022**, *14*, 9882.
[40] Y. Lu, J. Wang, L. Yu, L. Kovarik, X. Zhang, A. S. Hoffman, A. Gallo, S. R. Bare, D. Sokaras, T. Kroll, V. Dagle, H. Xin, A. M. Karim, *Nat. Catal.* **2018**, *2*, 149.
[41] Y. Fang, X. Chi, L. Li, J. Yang, S. Liu, X. Lu, W. Xiao, L. Wang, Z. Luo, W. Yang, S. Hu, J. Xiong, S. Hoang, H. Deng, F. Liu, L. Zhang, P. Gao, J. Ding, Y. Guo, *ACS Appl. Mater. Interfaces* **2020**, *12*, 7091.
[42] J. Huang, Y. Kang, L. Wang, T. Yang, Y. Wang, S. Wang, *Catal. Commun.* **2011**, *15*, 41.
[43] S. Jeong, G. M. Kim, G. S. Kang, C. Kim, H. Lee, W. J. Kim, Y. K. Lee, S. Lee, H. Kim, H. K. Lim, D. C. Lee, *J. Phys. Chem. C* **2019**, *123*, 29184.
[44] D. Gamarra, A. Martínez-Arias, *J. Catal.* **2009**, *263*, 189.
[45] L. Lukashuk, N. Yigit, R. Rameshan, E. Kolar, D. Teschner, M. Hävecker, A. Knop-Gericke, R. Schlögl, K. Föttinger, G. Rupprechter, *ACS Catal.* **2018**, *8*, 8630.